Article

Contrast-Enhanced, Molecular Imaging of Vascular Inflammation in the Mouse Model by Simultaneous PET/MRI

Siyi Du[1§]; Thomas S.C. Ng[2‡§], MD, PhD; Adrian House[3†]; Tang Tang[1††], PhD; Lin Zheng[4], PhD; Chuqiao Tu[3], PhD; Janice Peake[5], Imelda E. Espiritu[5], Kwan-Liu Ma[4], PhD; Kent Pinkerton[5], PhD; Russell E. Jacobs[2#], PhD; Angelique Y. Louie[1,3*], PhD

[1]Chemistry Graduate Group, University of California, Davis, United States of America

[2]Division of Biology & Biological Engineering, California Institute of Technology, United States of America

[3]Department of Biomedical Engineering, University of California, Davis, United States of America

[4]Department of Computer Science, University of California, Davis, United States of America

[5]Department of Anatomy, Physiology and Cell Biology School of Veterinary Medicine, University of California, Davis, United States of America

[†] current address: School of Medicine, Boston University, United States of America

[‡] current address: Department of Radiology, Brigham and Women's Hospital, Harvard Medical School, United States of America

[††] Cancer Research Center, Sanford Burnham Prebys Medical Discovery Institute, United States of America

[#] current address: Keck School of Medicine, USC, United States of America

*Corresponding author E-mail: aylouie@ucdavis.edu; Tel 530-752-7134

[§]both authors contributed equally to this work

Abstract: Despite advances in diagnosis and management, cardiovascular diseases (CVDs) remain the leading cause of death in the US. Atherosclerosis is the most common form of CVD and the vulnerability of atherosclerotic plaques to rupture is a primary determinant for risk of catastrophic ischemic events. Current imaging of atherosclerotic disease focuses on assessing plaque size and the degree of luminal stenosis, which are not good predictors of plaque stability. Functional methods to identify biomarkers of inflammation in plaques could facilitate assessment of plaque instability to allow early intervention. In this study, we validate the use of a purpose-built, magnetic resonance imaging (MRI)-compatible positron emission tomography (PET) insert for multimodal, molecular imaging of vulnerable plaques in mice. We illustrate the application of PET to screen for inflamed regions to guide the application of MRI. Molecular MRI visualizes regions of vascular inflammation and is coupled with anatomical MRI to generate detailed maps of the inflammatory marker within the context of an individual vessel. As a testbed for this imaging methodology, we developed a multimodal, iron oxide nanoparticle (NP) targeting vascular cell adhesion molecule-1 (VCAM-1) for simultaneous PET/MRI of vascular inflammation performed on a mouse carotid ligation model. *In vitro* cell studies confirmed that the NPs are not cytotoxic to liver cells. *In vivo* simultaneous PET/MRI imaging identified regions of inflammation. Three-dimensional rendering of the MRI data facilitated high-resolution visualization of patterns of inflammation along the injured vessel. Histology validated the co-localization of the NPs with VCAM-1 expression at sites of induced inflammation. The results of this work validate the utility of the simultaneous PET/MR insert as a research tool for small animals and lays groundwork to further advance the potential clinical utility of integrated imaging systems.

Keywords: Multimodality imaging; MRI/PET; dual-mode imaging; nanoparticle; atherosclerosis; vulnerable plaque; cardiovascular imaging; vessel wall; VCAM.

1. Introduction

47   Cardiovascular disease is the leading cause of death for both males and females in the United
48 States.[1] In particular, atherosclerosis is responsible for catastrophic manifestations of heart disease
49 such as myocardial infarction and stroke.[2] Recent understanding of the pathophysiology of
50 plaque formation has identified chronic inflammation as a hallmark of plaque development;
51 localized inflammatory response can lead to the development of "vulnerable" plaques that are
52 prone to rupture and cause downstream vascular occlusion.[3] Imaging can play a role in
53 identifying patients with vascular lesions susceptible to acute cardiovascular events, who may be
54 amenable to treatment with anti-inflammatories or interventional procedures. Recent literature has
55 shown that plaque lesion composition, particularly the presence of inflammatory markers and
56 immune cells, as opposed to the degree of vessel stenosis, is a better predictor of patient mortality
57 and morbidity; and assessment of plaque inflammation is an excellent target for noninvasive
58 imaging.[4] However, current clinical imaging techniques seldom provide specific information
59 about inflammation.

60   Current clinical imaging techniques such as coronary angiography, vascular ultrasound and
61 computed tomography focus on identifying stenotic disease and can miss vulnerable plaques that
62 do not cause significant structural stenosis.[5] Anatomical features identified by coronary computed
63 tomography (CT) and magnetic resonance imaging (MRI) that could be used to classify plaques,
64 have not been fully validated for prediction of vulnerability.[6] Targeted molecular imaging has
65 potential for greater predictive value. For example, imaging of plaque inflammation has been
66 actively pursued using ^{18}F-labeled fluorodeoxyglucose (FDG) positron emission tomography (PET)
67 and has shown promise for identifying inflammation, generally in large vessels such as the carotid
68 and aorta.[7-10] However, it is challenging to accurately assess inflammatory burden in small
69 vessels with the limited resolution of PET.[11] Moreover, FDG is a non-specific marker of
70 inflammation that measures only glucose uptake, which presents challenges for coronary artery
71 imaging against the high metabolic background of the myocardium.[12] Enthusiasm for the clinical
72 use of ^{18}FDG to identify plaques has diminished over recent years with new tracers such as ^{18}NaF
73 receiving greater attention; but specific imaging of plaque inflammation is still not available.[13]
74 New, targeted imaging strategies that can identify inflamed plaques in smaller vessels, such as the
75 coronary arteries, with higher specificity are needed.

76   We have previously shown that multimodal agents combining positron emission tomography
77 (PET) and magnetic resonance imaging (MRI) can detect macrophage density in plaques, using the
78 quantitative ability of PET for high sensitivity mapping of the cells, and MRI for high spatial
79 resolution molecular imaging and soft tissue mapping.[14] Our previous work utilized separate
80 scanners to visualize the synergistic PET and MRI information. This required laborious spatial
81 co-registration (prone to misalignment since they are acquired sequentially), more involved
82 handling of subjects with longer sedation, and time delay due to the need for transport between
83 PET and MR scanners. The latter factor also prevents temporal co-registration of the PET and MRI
84 signals. Not only does this hinder throughput of preclinical research pursuits, but also may limit
85 the translatability of such agents to the clinic. The use of hybrid modality instruments for
86 simultaneous signal acquisition is, thus, of increasing interest in the imaging field and clinical
87 hybrid instruments are now available; but the ideal cardiovascular applications for these hybrid
88 systems are still under investigation.[15]

89   In this proof of concept study, we demonstrate the utility of simultaneous PET and MRI to
90 facilitate PET-guided MRI mapping of localized inflammation in small vessels using an integrated
91 small animal simultaneous PET/MRI imaging system developed at UC Davis and a dual-mode
92 contrast agent targeted to Vascular Cell Adhesion Molecule 1 (VCAM-1).[16, 17] Vascular Cell
93 Adhesion Molecule VCAM -1 has received attention for imaging of atherosclerotic plaques due to
94 its overexpression in the pathogenesis of vulnerable plaques. It has been studied for single modality
95 imaging by MRI[18], SPECT[19, 20], and ultrasound[21]. Each of these modalities holds inherent
96 limitations for targeted vascular imaging. MRI and ultrasound can provide excellent local, spatial
97 information at the lesion site, but are ill-suited to whole-body screening. PET is superior for
98 screening, but lacks the spatial resolution to identify individual vessels. While computed

99   tomography (CT), can provide structural information, but does not provide physiological
100   information at the lesion site. MRI/PET has the potential to overcome these difficulties by
101   combining the screening power of PET with the resolution power of MRI, enabling concurrent
102   assessment of cardiovascular structural and physiological abnormalities.[22] We evaluated the
103   ability of the integrated PET/MRI instrument to visualize sites of localized inflammation induced by
104   carotid injury in a mouse model; the mouse carotid is of similar size to human coronary arteries.
105   PET provided an overview of inflamed regions, which was used to focus MRI interrogation and
106   obtain higher resolution, 3-dimensional details of VCAM-1 expression in single vessels.

2. Results and Discussion

108   Nanoparticles (NP) were successfully synthesized (outlined in Figure 1 and described in
109   Methods).

110   **Figure 1.** Synthesis of VDIO-DOTA nanoparticles. (a) Synthesis of dextran coated iron oxide
111   nanoparticle (b) Conjugation of DOTA and VCAM-1 targeting peptides to nanoparticles.

112
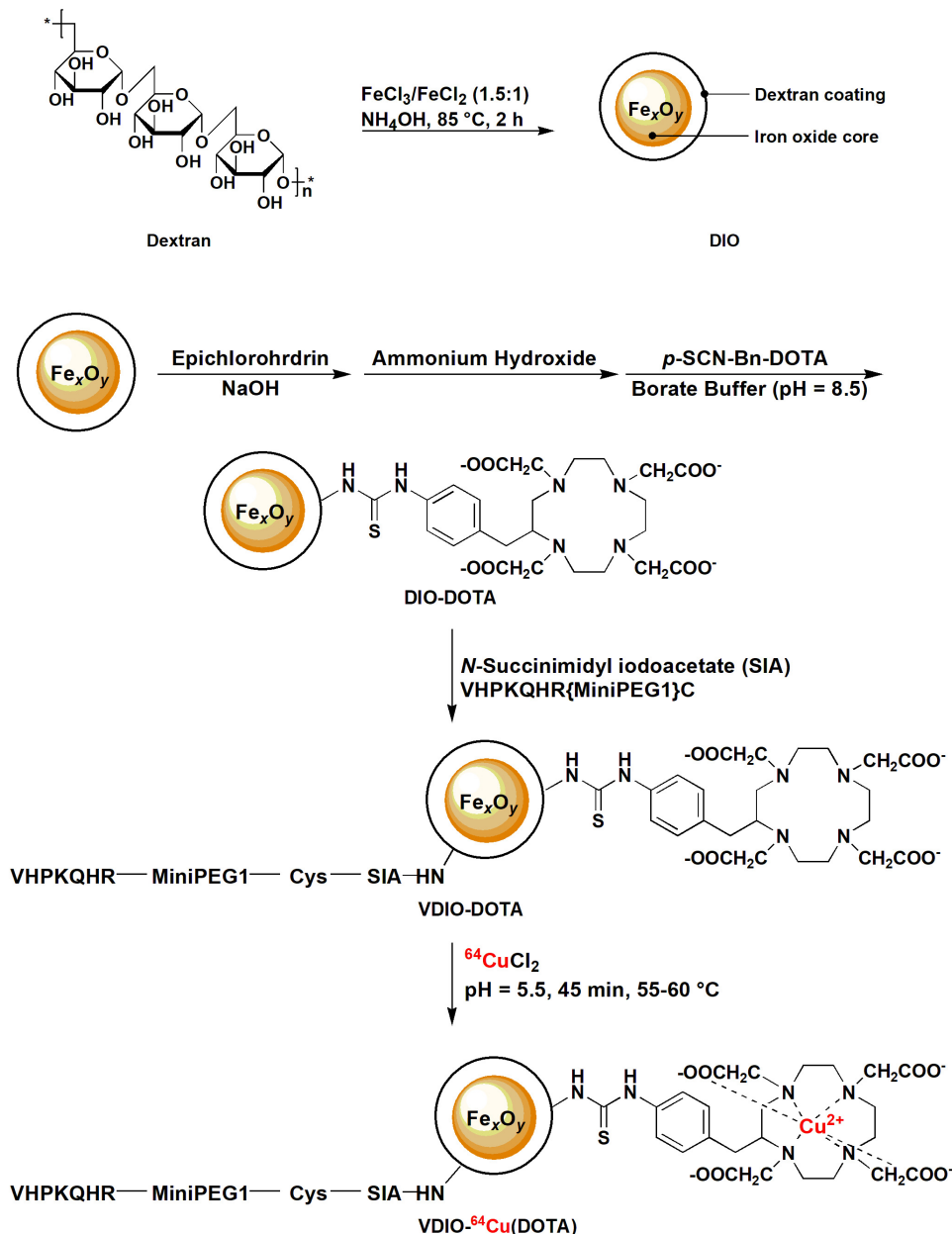
113   *2.1 Characterization of VDIO-DOTA and DIO (control)*

114   DIO (dextran-coated iron oxide) was synthesized as a matched control to the prepared
115   VDIO-DOTA (DOTA= 1,4,7,10-Tetraazacyclododecane-1,4,7,10-tetraacetic acid; VDIO=
116   VCAM-conjugated DIO;). The physical properties of VDIO-DOTA and its precursor DIO are
117   summarized in Figure 2a. Following the syntheses described, the DIO and VDIO-DOTA iron oxide
118   core sizes were measured to be 7.3 ± 2.9 nm by averaging 500 particle measurements from TEM
119   images as shown in representative images in Figure 2b and 2c. Inset plots show that the
120   hydrodynamic diameters of DIO and VDIO-DOTA were found to be 39.7 ± 15.0 nm and 48.1 ±
121   19.5nm, respectively, using dynamic light scattering (DLS). The increased hydrodynamic diameter
122   could be explained by the addition of peptide polymers on the VDIO surface holding the dextran
123   polymers apart via steric hindrance. However, the core sizes remained the same.

124   **Figure 2.** (a) Summary of nanoparticle properties. TEM images of (b) DIO (core size: 7.30 ± 2.92nm)
125   (C) VDIO-DOTA (core size: 7.30 ± 2.92nm). Scale bars = 50 nm, insets are DLS data.

| Nanoparticles	Core size (nm)	Average hydrodynamic diameter (nm)	Relaxivity (mM^{-1}s^{-1}) (1.4 T, 37°C)		% Iron
			r$_1$	r$_2$	
VDIO	7.30 ± 2.92	48.10	7.38	67.85	21
DIO	7.30 ± 2.92	39.7	10.05	68.83	16

(**a**)
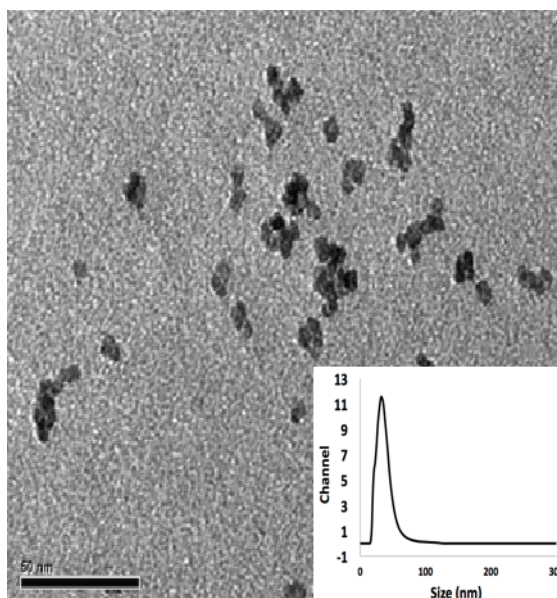
(**b**)
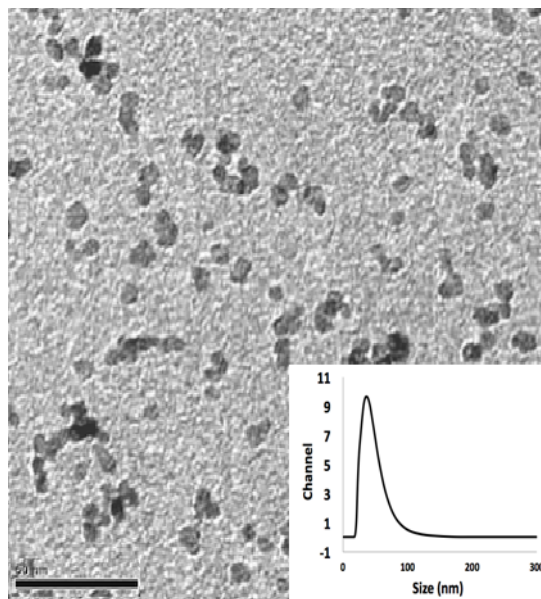
(**c**)

126   The iron concentration (mg per unit mass) in DIO and VDIO-DOTA was measured by atomic
127   absorption (AA) to be 0.161 and 0.037 mg Fe/mg of nanoparticles, respectively. The longitudinal (r_1)
128   relaxivity of VDIO-DOTA at 60 MHz (1.4 T, 37 °C, pH = 7) was 7.4 mM^{-1}s^{-1} and transverse relaxivity
129   (r_2) was measured as 67.9 mM^{-1}s^{-1}. DIO had r_1 and r_2 values of 10.1 mM^{-1}s^{-1} and 68.8 mM^{-1}s^{-1},
130   respectively. The r_2 to r_1 ratio for both reflects their suitability as T_2-weighted MRI contrast
131   agents.[17] VDIO-DOTA relaxivity and size remained stable after 1 year of dry storage at room
132   temperature.

133   *2.2 Contrast Agent is Not Cytotoxic to Liver Cells in vitro*

134   Given that NPs are expected to clear through the liver, liver cells may be exposed to the
135   highest off-target concentration of injected contrast agent. Thus, C_{12} – Resazurin viability assays
136   were performed on HepG2 liver cells to evaluate any toxicity exhibited by VDIO-DOTA.[23] In this
137   assay resazurin is reduced to resorufin in proliferating cells.[23] Cell survival was evaluated after
138   incubation for 4, 24, and 48 hours with different concentrations of VDIO-DOTA, ranging from 0.04
139   mM iron (red), 0.2 mM iron (blue), 1 mM iron (teal), 4 mM iron (pink) to 10 mM iron (khaki). With
140   90% confidence interval by t-test there were no differences between the untreated control (0.0 mM
141   iron, black) and cells treated at all concentrations of VDIO-DOTA tested from 0.04 mM iron up to 10
142   mM iron. These results support that the nanoparticles are nontoxic to liver cells at relatively high
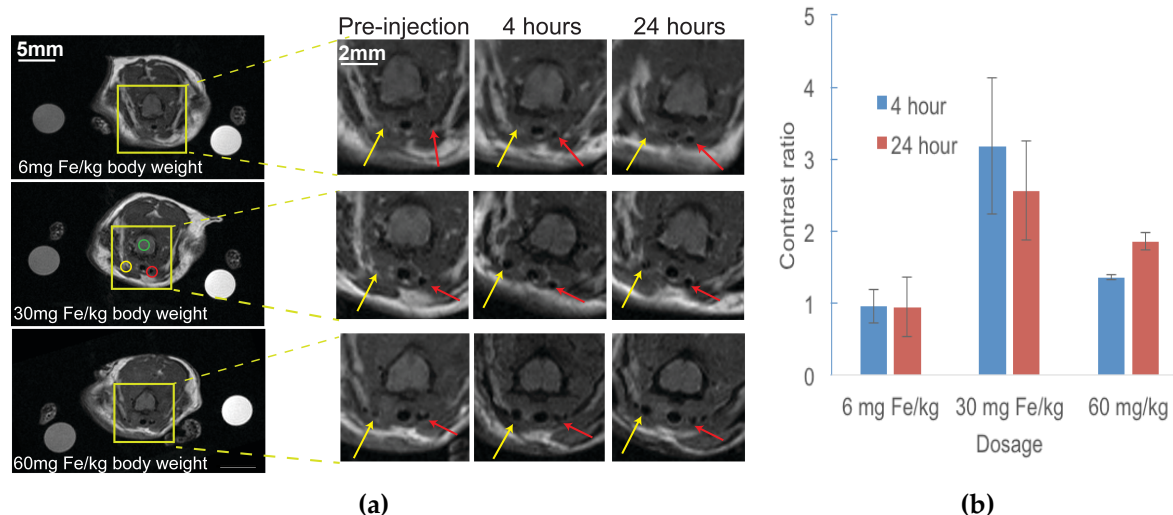143   concentrations.
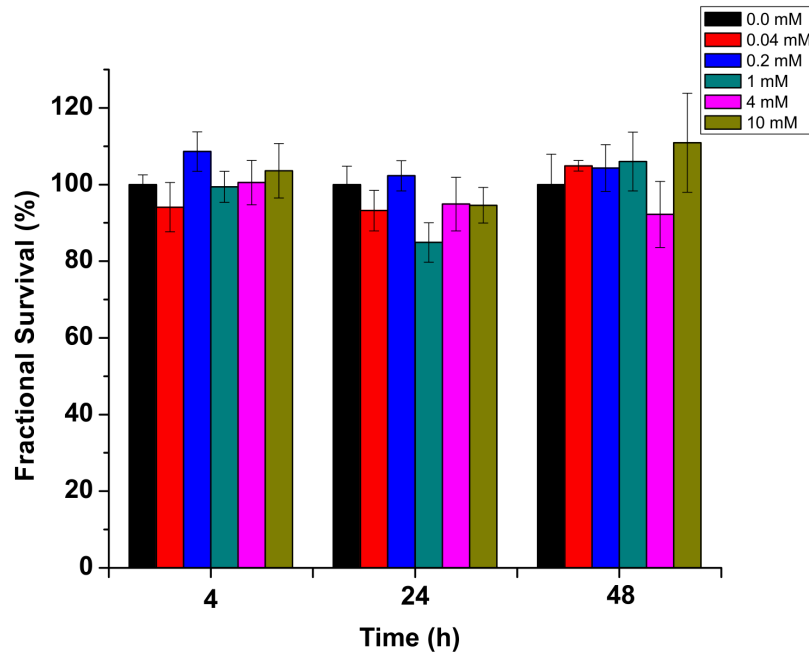
Figure 3. The fractional survival of HepG2 after 4, 24 and 48 hours of incubation with VDIO solutions of varying concentrations. At each time point, fluorescent intensities reflecting survival fractions (y axis) were normalized against the signal from the untreated control group (black bar at each time point).

2.3 VDIO-DOTA can to detect inflamed vessels in vivo

MRI only studies were performed to determine appropriate dosing prior to PET/MRI studies. Representative MRI scans showing VDIO-DOTA uptake at the three injection concentrations are shown in Figure 4a (n = 4 mice per concentration). The leftmost column shows cross sections through the entire animal for, from top to bottom 6mg/ml, 30mg/ml and 60 mg/ml injection of nanoparticles. These are labeled with colored circles to indicate the injured vessel (yellow circle), uninjured contralateral vessel (red circle) and spinal cord (green circle). The co-registration standards are also visible to left and right of the animal. The regions outlined by the yellow boxes are presented in zoomed views on the matrix of images on the right, which show, from left to right, images from this region taken pre-injection, and images 4 and 24 hours after injection of contrast. For all concentrations, the inflamed vessel (yellow arrows) showed expected increased dephasing (seen as signal dropout) as the concentration of VDIO-DOTA injected is increased resulting in greater accumulation at the ligated site compared to the nonligated contralateral vessel (red arrows). This darkening in the inflamed arteries persists through the 24h timepoint for all concentrations, showing sustained retention of the particles at the site of inflammation. Robust signal for 6ml/ml suggested that even lower injection concentrations could be employed. The CR was calculated as a function of time after injection and dosage and shown in the accompanying graph in Figure 4b. Although the 60 mg Fe/kg dose showed the greatest signal decrease on the images, maximal CR was achieved with the 30 mg Fe/kg dosage at both 4h and 24h after injection of contrast. This highlights the need to achieve a balance between local accumulation of the NP, retention over time, and its systemic circulation for optimal visualization of the region of interest. Using these results as a guide, 30mg Fe/kg was used for the remainder of the studies.

(a)   (b)

Figure 4. (a) MRI-only study showing VDIO-DOTA uptake at different injection concentrations over 24 hours. The yellow arrows point to the inflamed vessel, while the red arrows indicate the non-inflamed control vessel. There was signal decrease at the site of injury at all dosages; but the decrease was most prominent at the 30 and 60 mg Fe/kg. The regions of interest for Contrast Ratio (CR) calculation are shown by the circles. (Scale bar = 5 mm). (b) Contrast ratio as function of time and dose for MRI-only studies. Compared to baseline, the 6 mg Fe/kg dose level did not demonstrate significant local accumulation of NP at the site of inflammation. Both the 30 mg Fe/kg and 60 mg Fe/kg showed increased accumulation of NP at the site of inflammation; the 30 mg Fe/kg dose demonstrated the highest CR, likely due to the reduction of signal differentiation between the localized accumulation and systemic distribution of NP at the 60 mg Fe/kg dosage. Thus the 30 mg Fe/kg dose was used for subsequent studies. (Error bars denote the SEM).

Following these MRI only studies, we evaluated VDIO-^{64}Cu-DOTA nanoparticle accumulation *in vivo* by hybrid PET/MRI. Figure 5 shows image slices by MRI (top row), by PET (middle row) and the overlay (bottom row) from the same cross section in a representative mouse (n = 4 mice total). Prior to injection of VDIO-^{64}Cu-DOTA, no MR or PET signal beyond background levels was seen within the animal. At 4 h post injection, both carotids demonstrated PET signal, which was higher in the injured vessel, suggestive of radiolabeled NP accumulation at the site of injury along with continued systemic circulation of unbound NP. Another focus of PET uptake within the field of view appear to correspond with a vein, supporting that systemic circulation of the NP remains at this time point, but which could represent another site of inflammation in the animal. In the slice shown, at 4 h there is a signal increase in the ligated vessel (yellow arrow) at a ratio of 1.19 compared to the uninjured contralateral vessel; at the 24 h time point the ratio of the ligated site compared to the contralateral artery was 1.07; partial volume effects limits the accuracy of these measurement. We also calculated the MRI contrast ratio (CR; see equation in methods 4.6.3) from the concurrent MRI dataset. Note that CR also is a comparison against the contralateral control, thus taking into account contributions from signal in the blood. For this particular animal, the MRI CR was 1.41 at the 4 h time point and 0.62 by 24 h, indicating elevated NP accumulation at the ligated site at the 4 h timepoint with decreased MRI signal by 24 h, commensurate with the PET results. This slice was selected to illustrate the point that these trends are for this slice, in this particular animal and based on this slice only one may conclude there was no inflammation in this vessel. For a more accurate view of inflammation the entire affected volume should be considered, as well as the full set of experimental subjects. As shown later, mapping inflammation throughout the vessel provides a clearer picture of inflammatory burden. The MRI CRs for the entire PET/MRI cohort were 1.65 ± 0.26 at 4 h and 1.66 ± 0.39 at 24 hours respectively. In general, this is in agreement with the data for the MRI only cohort, which also demonstrated an increased MRI CR over the 24 h period (Figure 5b). Note that these results support that ligation does not prevent contrast agent

207 access to the injured carotid—if this had been the case there would be less signal drop out due to
208 reduced perfusion to the region.

209
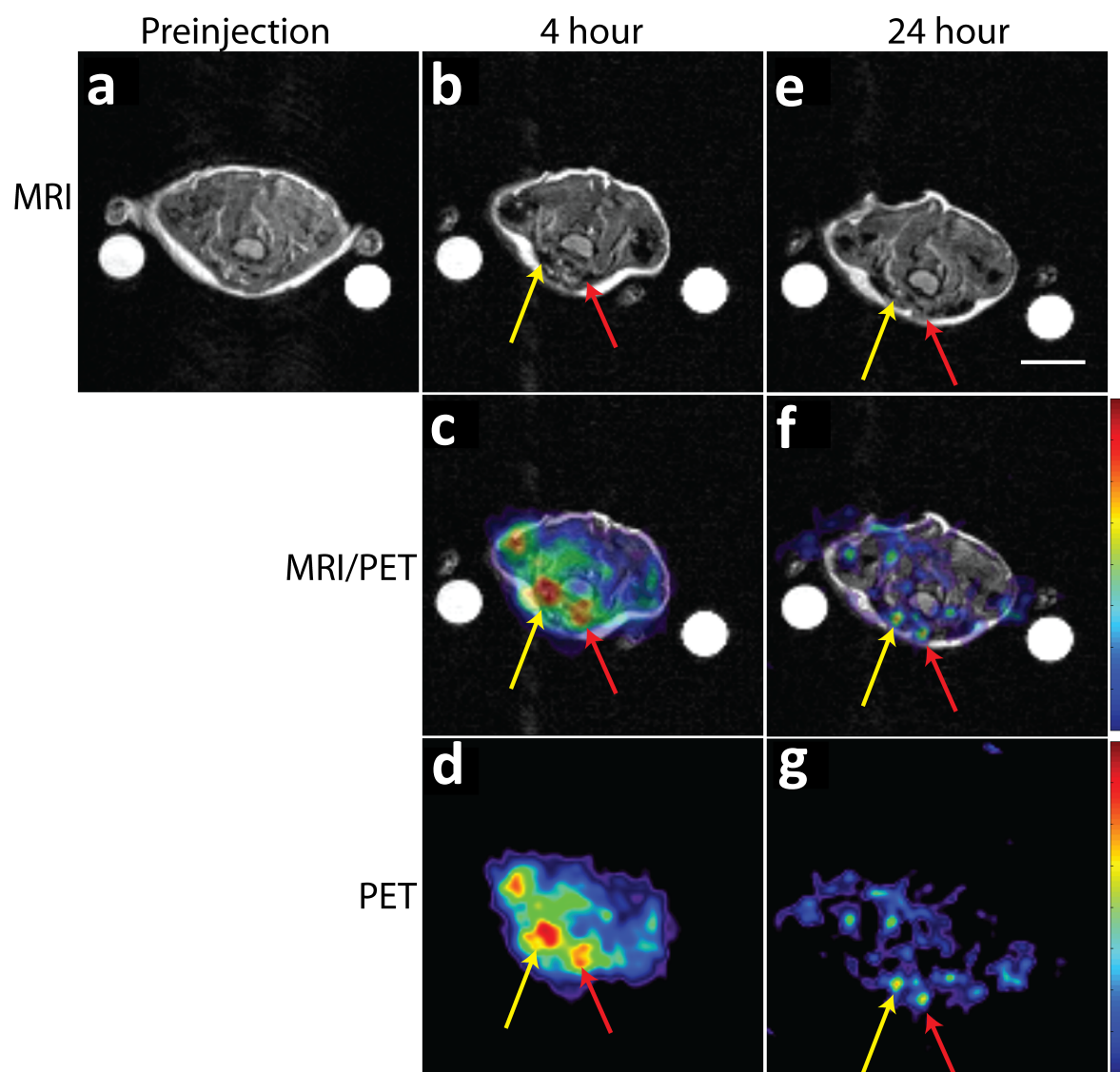
Figure 5. PET/MR imaging of dual-mode VDIO-DOTA accumulation in carotid artery of ApoE^{-/-} mouse with vascular inflammation (atherosclerotic plaques) induced by ligation. MRI-only images preinjection (a), after 4h(b) and 24h(e) injection, PET/MRI co-registered images after 4h(c) and 24h(f) injection and PET-only images after 4h(d) and 24h(g) injection are shown. The image slices were from the same cross section of the mouse and showed spinal cord (grey oval area in the middle), left carotid (after ligation) artery (denoted by yellow arrow) and right carotid artery (denoted by red arrow). The color maps for the PET images were set such that the highest values (as indicated by red) reflected the highest signal within the animal image volume for the particular time point. The white circles are markers for MRI intensity standards. (Scale bar = 5 mm).

219 The lower resolution of PET provides decreased accuracy in determining inflamed regions due
220 to partial volume effects, and subtle inflammatory lesions may be missed. This is suggested by the
221 fact that although analysis of the MRI data suggested there was accumulation of the NP at the
222 ligated site, this was not reflected by the simultaneously acquired PET data. The ratios of the PET
223 signal at the ligated artery compared to the control artery were 1.05 ± 0.04 at 4 hours and 0.82 ± 0.33
224 at 24 hours. This highlights the need for high-resolution 3D renderings of the affected volume to
225 better identify regions of high inflammatory activity and assess degree of instability. For improved
226 volume visualization, we performed three-dimensional rendering of the MRI data as shown in

227 Figure 6. MRI rendering is able to define regional accumulations and concentration differences for
228 VDIO-DOTA in the vessel wall, allowing us to better localize VCAM-1 expression to specific
229 regions in the inflamed vessel. Figure 6a and b show rendering of the MRI only data from the 30 mg
230 Fe/kg dose injection for a representative animal, with a slice from the anatomical MRI included for
231 anatomical context; this is the same animal and slice view used for the cross section image shown in
232 Figure 4. The color map (transfer function) for the image was set to define three major color zones
233 representing low (red), medium (blue), and high (pink) NP uptake. Greater susceptibility from
234 T_2-weighting indicates regions of greater particle accumulation (more red). The volume renderings
235 suggest that VCAM-1 expression, which is targeted by the NPS and indicative of activated
236 endothelial cells and inflammation, is diffuse along the vasculature and that expression patterns
237 vary across the vessel. In this particular animal there is a greater accumulation of contrast agent on
238 one side of the vessel as seen in the 4 h still images in panel a. At 24h (panel b) the trend persists
239 and one can observe accumulation on one side that is consistent with the 4-hour data.

240 **Figure 6.** Three-dimensional rendering of MRI data (a – b). Medium dose study, MRI data (from
241 Figure 3). (a) Still frames from video depicting a rotating view of the inflamed vessel 4 h after
242 injection of contrast agent. (b) Similar data for the vessel at 24 h. A similar trend for higher
243 accumulation of contrast agent on one side of the vessel is preserved at both time points. (c – d)
244 PET/MRI study, MRI data (From Figure 4). (c) Still frames from video depicting a rotating view of
245 the inflamed vessel 4 h after injection of contrast agent. (d) Similar data for the vessel at 24 h. A
246 trend for a "hot spot" (red) accumulation of contrast agent at the same location is seen at both time
247 points.   Transfer functions used for color assignments are displayed as color bars shown between
248 the 4 and 24h data sets.
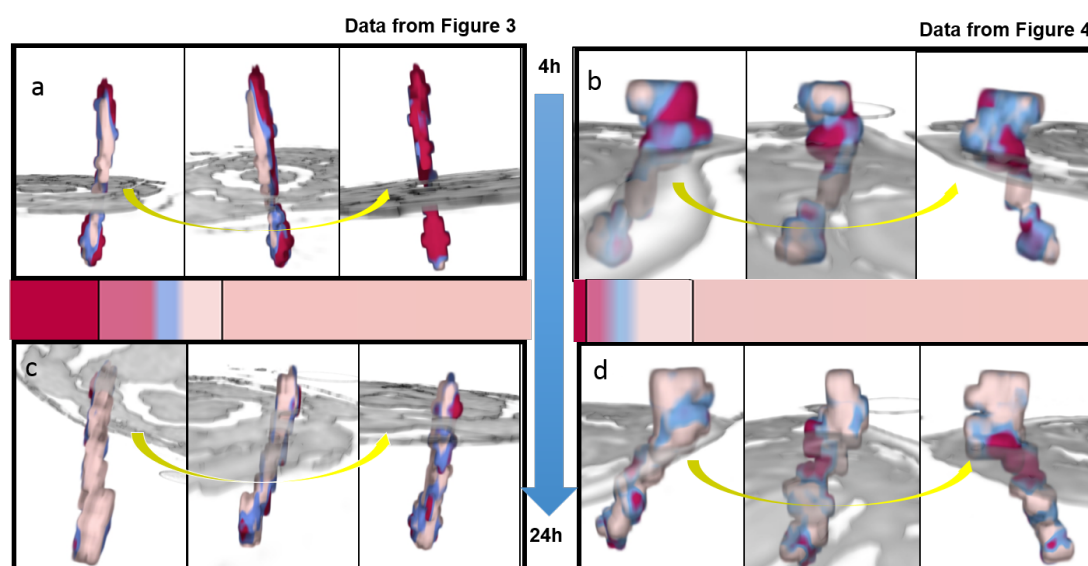
250 Figures 6c and d display rendering of the MRI data for the animal shown in the PET/MRI
251 images of Figure 5. Inflammation is even more heterogeneous in this animal and NP accumulates in
252 patches throughout the vessel. A local "hot spot", appears in the 4 h data (panel c) and persists but
253 is decreased through the 24 h time point (panel d) commensurate with the PET and MRI CR results.
254 At 24 h most of the hot spot lies below the plane of interrogation that was show in the slice in
255 Figure 4; this may explain the lack of PET observed in the slice shown and also underscores the
256 value of evaluating 3D data sets as volume renderings. The rendering provides insight into the
257 heterogeneity of the NP accumulation, which is not readily apparent from slice by slice
258 visualization of the MRI image set. This data correlates with the histological data, described in the
259 next section, which showed inhomogeneous regional accumulations of the nanoparticles that
260 overlap with regions showing high VCAM-1 expression. The morphology of the local plaque load
261 can have prognostic implications.[24] Thus, this additional information from the high resolution
262 MRI may provide vital information for clinical management.

263   The addition of a 3D visualization is very useful for interpreting these types of data sets where
264   the disease is diffuse and lesions can span across multiple slices. One of the challenges for 3D
265   rendering is the ability to create images and videos without the need for extensive manual
266   segmentation, i.e. user delineation of pathology. The renderings shown here were created using
267   software created at UC Davis that performs intensity-based segmentation by applying a
268   user-defined color map to all voxels in the data set. This removes some degree of subjectivity from
269   the assignment of pathological features.

270   *2.4 Iron co-localizes with VCAM-1 expression*

271   Mice were sacrificed after *in vivo* MRI only or PET/MRI study and organs of interest were
272   collected for further analysis. For the MRI only studies, the tissues from mouse carotids were
273   embedded into paraffin sections for histological study to examine iron accumulation (Figures 7a, c,
274   e) and VCAM-1 expression (Figures 7 b, d, f) in the tissues. Prussian Blue staining was used to
275   detect ferric ion (Fe^{3+}) in the tissue. As shown in Figure 7a blue staining demonstrated that iron
276   could be found in the intima in the inflamed carotid artery (arrow). Anti-VCAM-1 antibody
277   staining was performed on an adjacent section (Figure 7b), which confirms the presence of VCAM-1
278   in the same region, as indicated by dark brown stain of the intima on the left side of the vessel
279   lumen (arrow). The dark blue iron staining co-localized in the regions of darkest brown VCAM-1
280   staining, supporting that the nanoparticles were co-localized with VCAM-1 expression. There
281   appears to be a thin layer of VCAM-1 staining on the rest of the lumen that does correlate with
282   some iron staining. The faint brown stain over the entire intima represents nonspecific staining that
283   is also found in the control vessel. Non-inflamed contralateral vessel showed no iron (Figure 7c) or
284   dark brown VCAM staining (Figure 7d).
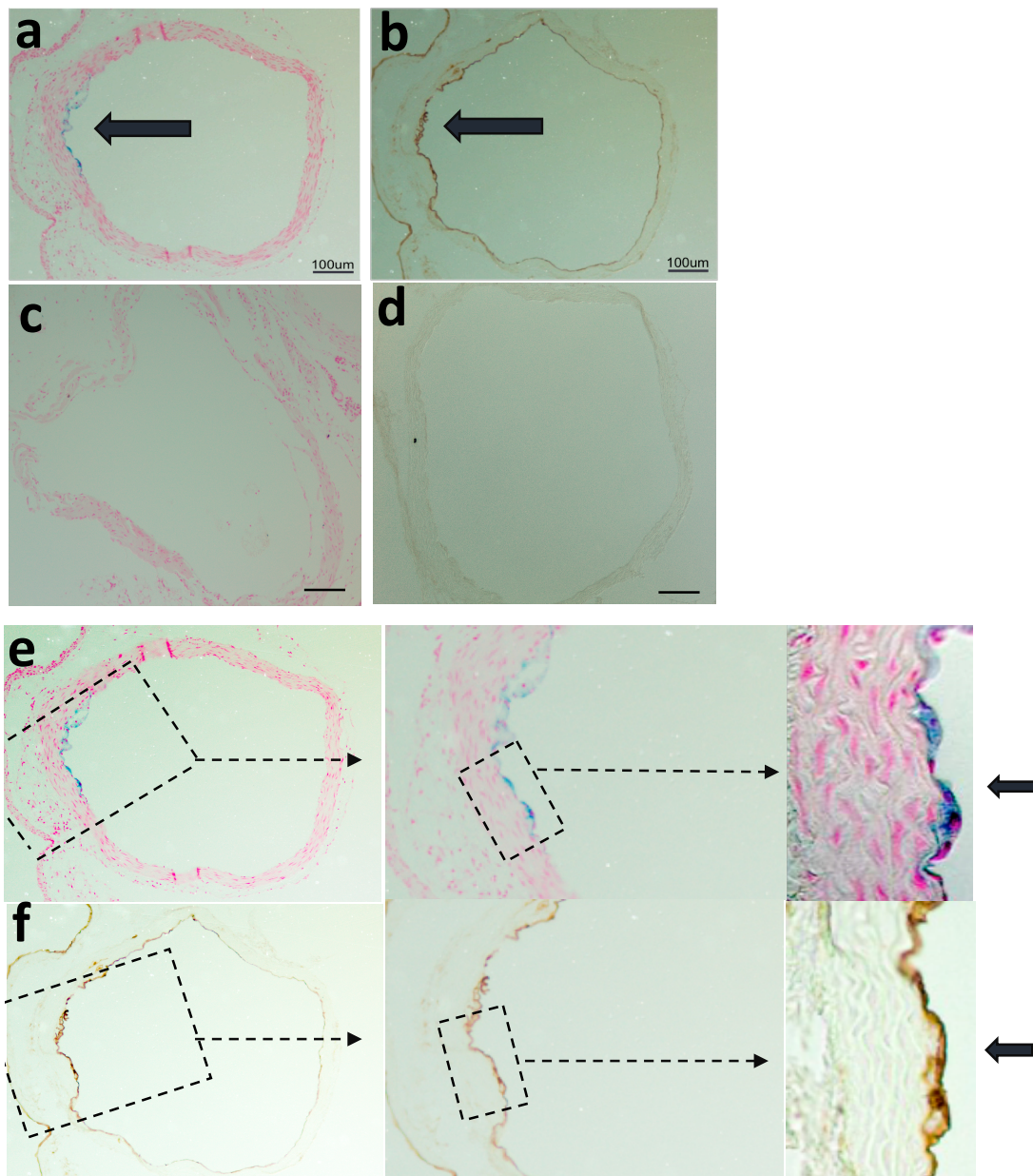
Figure 7. Iron colocalizes with VCAM-1 expression. (a). Prussian Blue staining hows iron on tissue cross section from inflamed mouse carotid artery. (b). Immunohistochemical staining shows VCAM-1 (brown) on a tissue slice adjacent to that shown in A. (c). Prussian Blue staining showed no iron in tissue cross section from normal mouse carotid artery and (d) no VCAM-1 staining on neighboring tissue slice. (e) Higher magnification view of Prussian Blue staining in panel a at 10X, 20X and 40X. (f) Higher magnification views of VCAM-1 staining in panel b. Dashed boxes indicate the area of interest with increasing magnification, moving left to right. Staining appears localized to the monolayer of endothelial cells lining the vessel.

VCAM-1, triggered by inflammatory cytokines such as TNF-α, is expressed by endothelial cells as a prelude to the recruitment of macrophages into plaques. In our previous work to label macrophages in the injury model, animals were placed on fat diet for 2 weeks after ligation; the current studies were performed 8 days after ligation. At this earlier time point, plaque size and macrophage involvement are minimal as can be seen in the higher magnification histological images. Figure 7e shows iron staining at increasing magnifications from left to right and iron

300 staining localized to cells of the intima, which is still generally a monolayer of endothelial cells.
301 Figure 7f shows VCAM-1 staining at increasing magnifications from left to right, which shows
302 VCAM-1 localized to the same monolayer. There was no intimal thickening, or obvious
303 macrophage accumulation observed in the histological slices. The iron stain also appeared confined
304 to a monolayer of "cobblestone-like" endothelial cells and there was no evidence of macrophages,
305 which display surface ruffles and blebs. These results support that the NPs were binding to
306 VCAM-1 expressed on endothelial cells.

307 **4. Conclusions**

308 In this study, we evaluated the use of a simultaneous hybrid PET/MRI system and multimodal
309 nanoparticle contrast agent to visualize distribution of an early marker of inflammation. We found
310 robust spatial-temporal co-localization of the PET and MRI signal, and identified regions of
311 inflammation, which were confirmed by histological staining. PET, limited by its lower spatial
312 resolution, could not specifically map inflammation in the vessels. PET also missed elevated
313 contrast that was detected by MRI, likely due to signal averaging effects of diffuse inflammation in
314 the tissues. But the sensitivity of PET allowed detection of inflammation in a larger volume map
315 and served to guide MR imaging. Careful analysis of the MRI data, aided by 3D volume rendering,
316 demonstrated a heterogeneous pattern of VCAM-1 expression extending beyond the site of vessel
317 injury. The morphology of the local inflammation patterns can have prognostic implications.[24]
318 This high-resolution mapping of early stage inflammation would not have been possible with MRI
319 alone as lesions are difficult to detect in small vessels against anatomical background. Whole body
320 MRI screening in humans would be even more challenging. Thus, the combination of PET and MRI
321 provided complementary functions in this imaging application.
322 Simultaneous PET/MRI imaging of the multimodal NP afforded a number of advantages over
323 serial imaging including: 1) avoiding movement of the subject between scanner-, which allowed for
324 facile spatial co-registration to do the lack of soft tissue movement experienced with scanning with
325 separate instruments; 2) eliminating time delay between PET and MRI scans, which avoided
326 complications with subject transport under anesthesia; 3) reduced exposure to personnel associated
327 with handling and transporting the subject between instruments in different facilities. Given that
328 many high-resolution MRI techniques are often time consuming and have a limited field of view,
329 the availability of hybrid instrumentation can allow us to localize the ROI using PET without loss of
330 spatial fidelity that would come with moving the subject to a separate scanner. This would be
331 especially important in the clinical scenario whereby the site of injury may not be known a priori.
332 The approach of using hybrid PET/MRI instrumentation along with multimodal imaging
333 probes provides a powerful platform for both research and clinical pursuits. From a research
334 perspective, hybrid imaging can provide direct information about the efficacy and distribution of
335 multimodal molecular imaging agents, providing vital information to refine and improve the signal
336 characteristics of these agents. From a clinical perspective, PET/MRI hybrid instruments are
337 available now in a limited number of locations and their optimal applications are under
338 investigation. Oncological applications have been some of the earliest imaging studies to
339 demonstrate beneficial results from hybrid PET/MRI.[39, 40] For example, a study of PET/MRI for
340 clinical prostate cancer imaging found that PET/MRI may demonstrate improved sensitivity to
341 metastatic lesions compared to PET/CT.[41] Hope for improved diagnoses through hybrid PET/MRI
342 is high for neurological applications, where the temporal alignment of hybrid instruments could be
343 an advantage for examining brain processes in real-time.[16]
344 Cardiovascular applications that could benefit from PET/MRI are still under investigation [22,
345 42]; however, the simultaneous acquisition capability could offer advantages for imaging fast
346 moving hearts and arteries. Most reports with PET/MRI have focused primarily on unimodal
347 contrast agents such as [18]FDG using MRI as an anatomic reference.[15, 43, 44] We demonstrate that
348 PET-guided MRI using multimodal agents can facilitate high-resolution visualization of molecular
349 targets, and establish utility for mapping a marker associated with inflammation. This can serve as
350 a powerful research tool for drug validation by allowing monitoring of biomarker targets. Early

351 diagnosis and patient stratification by PET/MRI could provide clinical benefit as drugs to
352 ameliorate plaque vulnerability come available.

353   In summary, we have demonstrated an approach to identify early inflammatory changes in
354 vessel injury using a targeted multimodal probe coupled with hybrid PET/MRI imaging *in vivo*.
355 Such approaches may be able to provide important insights into the pathophysiology and clinical
356 management of vulnerable plaques. Furthermore, simultaneous PET/MRI allowed direct
357 comparison of the PET and MRI signal, providing insights into the signal derived from the
358 multimodal agent that can guide continued development of the instrument as well as the imaging
359 agent.
360

361 **5. Materials and Methods**

362 *5.1 Materials*

363   Materials were obtained from commercial suppliers and used directly, unless otherwise noted.
364 Dextran (from leuconostoc, average mol. wt. 9,000–11,000) and ferric chloride hexahydrate
365 ($FeCl_3 \cdot 6H_2O$, Fw 270.29 g/mol) were purchased from Sigma-Aldrich. Ferrous chloride tetrahydrate
366 ($FeCl_2 \cdot 4H_2O$, Fw 198.81 g/mol) was from Fluka. Ammonium hydroxide (28–30%), sodium
367 bicarbonate, and sodium hydroxide were from Fisher Scientific. p-SCN-Bn-DOTA was from
368 Macrocyclics, Inc (Dallas, TX). N-succinimidyliodoacetate (SIA), purchased from Pierce (Rockford,
369 IL). Spectra/por® dialysis membrane (mol. wt. cut-off 50,000) was acquired from Spectrum
370 Laboratories, Inc. The VHPKQHR(MiniPEG1)C peptide was from Genscript (≥ 95% purity). Water
371 was purified using a Millipore Milli-Q Synthesis purifier (18.0 MΩ cm, Barnstead).

372 *5.2 Nanoparticle synthesis and characterization*

373 5.2.1 Synthesis of dextran coated iron oxide (DIO) nanoparticles

374   Dextran was reduced by published methods as summarized here and outlined in Figure 1.[25]
375 Nanopure water (18.0 MΩ cm, Barnstead) was degassed with argon and used throughout the
376 synthesis process. A mixture of dextran (molecular weight 10,000) and sodium borohydride (26
377 equivalents) was stirred at room temperature for 12 hours. The solution was adjusted to pH=7,
378 dialyzed against degassed nanopure water and lyophilized to form reduced dextran as a white
379 solid. A mixture of reduced dextran and $FeCl_3 \cdot 6H_2O$ in a molar ratio of 1:27 (total polysaccharide:
380 $FeCl_3 \cdot 6H_2O$) was dissolved in deionized nanopure water. The solution was bubbled with argon and
381 cooled to 4 °C in an ice-water bath. Fe^{2+} solution was freshly prepared by dissolving $FeCl_2 \cdot 4H_2O$ in
382 degassed water (with a $Fe^{3+}:Fe^{2+}$ ratio in a range from 1.47 to 1.5) and stored on ice. The Fe^{2+} solution
383 was added to Fe^{3+} mixture using a syringe followed by adding chilled (4 °C) NH_4OH ($NH_4OH: Fe^{3+} =$
384 16:1) dropwise with vigorous stirring. The ice-water bath was removed and the mixture was heated
385 to 85 °C and kept at 85 ± 5 °C for 2 hours (argon flow may stop 2–3 min after the temperature
386 reaches 85 °C). After cooling to room temperature, the solution was dialyzed against deionized
387 water in a dialysis bag with a molecular weight cut-off of 50,000 Da for 72 hours with 8-10 changes
388 of water to remove reactants. The resulting product, DIO, was lyophilized and stored at 4 °C.[26]

389 5.2.2 Cross-linking and amination of the DIO nanoparticles

390   The DIO nanoparticles were cross-linked and aminated for the attachment of two ligands:
391 DOTA (chelator of radioactive ^{64}Cu) and the VCAM-1 targeting peptide (Figure 1). The
392 cross-linking and amination were performed as previously reported with slight modifications.[27]
393 DIO (2.0g), NaOH (4.02g) pellets and deionized water (40mL) were added to a 100mL
394 round-bottomed flask and stirred for 30 min. Then epichlorohydrin was added to the mixture and
395 the solution was stirred for 24h. The solution was dialyzed against deionized water with 8-10
396 changes of deionized water and lyophilized to yield brown solid. The solid (2.0 g), together with
397 ammonium hydroxide (250mL), was then transferred to a 500mL round-bottomed flask and stirred

398 for 36h. Excess ammonium hydroxide was removed by dialyzing the solution against deionized
399 water for 72h with 8-10 changes of deionized water.

400 5.2.3 Conjugation of DOTA and VCAM-1 targeting peptide to the nanoparticle surface

401 DOTA was conjugated to the aminated DIO surface based on a literature method. Briefly,
402 p-SCN-Bn-DOTA (6.71mg), aminated nanoparticle (135mg) and 0.1 M sodium borate buffer
403 solution (2mL) were added to a 10 ml round-bottomed flask (Figure 1b)[28]. Approximately five
404 drops of sodium hydroxide aqueous solution (1N) was used to bring the solution pH to 8.5. The pH
405 of the mixture was monitored during the reaction. The mixture was stirred for 24h, then dialyzed
406 against deionized water for 72h with 8-10 changes of water in a dialysis bag with a molecular
407 weight cut-off of 50,000 Da and then lyophilized to give a brown solid of DOTA conjugated
408 aminated DIO (DIO-DOTA). The conjugation of DOTA to the aminated DIO was confirmed by
409 Fourier Transform Infrared (IR) Spectroscopy. DIO-DOTA was then used for anti-VCAM-1 peptide
410 attachment based on previous report[29], described here briefly.
411 DIO-DOTA (22mg Fe in 1.5mL DMSO) was added to 0.5mL of 0.1M Na_2HPO_4 in water and
412 0.5mL of 15mM SIA in DMSO in a 10mL round-bottomed flask. The mixture was stirred for 1h at
413 room temperature followed by another addition of 0.5mL of 15mM SIA
414 (N-succinimidyliodoacetate) in DMSO. Iodoacetyl-DIO was separated from iodoacetic acid using a
415 Sephadex G-25 column equilibrated with 0.025M citrate buffer pH 6.5 at 4 °C. Then 6-7 mg of
416 polymer-modified peptide (VHPKQHR(MiniPEG1)C) in 0.6mL of citrate buffer was added to 5mL
417 of iodoacetyl-DIO solution and the mixture was incubated overnight at room temperature. The
418 purchased peptide, $C_{49}H_{84}N_{18}O_{14}S_1$, had a molecular weight of 1181.37 Da and an isoelectric point of
419 pH 9.84. MiniPEG1 (8-amino-3,6-dioxaoctanoic acid) spacer was inserted to distance the peptide
420 from the surface of the nanoparticle to allow for proper tertiary folded structure and allow better
421 VCAM binding. Unreacted peptide was removed by using a Sephadex G-25 column equilibrated
422 with 0.025M citrate buffer pH 6.5 at 4°C. The purified solution was lyophilized to give the final
423 product that is the DIO nanoparticle with two ligands (DOTA and VCAM-1 targeting peptide) on
424 the surface (VDIO-DOTA).

425 5.2.4 Copper-64 labeled VDIO-DOTA

426 Copper-64 was employed due to its relatively long half-life (12.7 h)[30] and comparatively
427 stable coordination with multidentate macrocyclic compounds such as DOTA (log K_{ML} = 22.3).[31]
428 VDIO-DOTA (25 mg) was dissolved in 150 μL of 0.2 M pH 5.5 sodium acetate-acetic acid buffer.
429 Copper-64 (~ 2.5 mCi) was added to the vial and the mixture was vortexed for 5 seconds to obtain a
430 uniform solution. The solution was incubated at 55-60 °C for 45 minutes. EDTA aqueous solution
431 (16 μL, 100 mM) was added to the vial and vortexed for 5 seconds to get the solution uniform; then
432 solution was incubated at 55-60 °C for 15 minutes. The crude product was purified by centrifuge
433 filtration with 10K Da nanosep filtration tube (Millipore Inc., Billerica, MA, 30 min @14,000 rpm)
434 and washed 3 times with pH 5.5 sodium acetate-acetic acid buffer. Each time the washing was
435 removed by centrifuge filtration with a 10-kDa Nanosep filtration tube (10 min at 14,000 rpm). After
436 three washings the filtration tube was turned over and inserted into a new vial, and the
437 nanoparticles, VDIO-^{64}Cu-DOTA, were collected by centrifuge (2 min @ 1,000 rpm). The radioactive
438 nanoparticles were diluted to 650 μL with saline (0.9%) and radioactivity of the solution was
439 measured with a Fluke Biomedical Dose calibrator (34- 162 CAL/RAD MARK IV, Cleveland, OH).
440 The radiolabeling yield (%) for the NP, percent incorporation of radioisotope, was determined by
441 dividing the radioactivity of the collected NP by the total activity applied to the column and
442 multiplying by 100. For injection to animals VDIO-^{64}Cu-DOTA (~ 15 μL) was passed through a
443 sterile 0.22-micron filter before use.

444 5.2.5 Characterization of VDIO-DOTA nanoparticles

445 The iron concentration (mg) per unit mass of nanoparticles in DIO or VDIO-DOTA was
446 measured with a Varian AA 220FS atomic absorption (AA) spectrophotometer using an
447 air/acetylene flame. The iron-oxide core size of the VDIO-DOTA was measured by Transmission
448 Electron Microscopy (TEM) on a Philips CM-12, operating at 80 kV and equipped with a
449 GatanMegascan 795 digital camera. The core size was found by averaging the measurements of 500
450 particles after drying a dilute drop of VDIO-DOTA particles over a lamp on a copper grid. The
451 average hydrodynamic particle size (mean volume diameter) and distribution was measured using
452 Dynamic Light Scattering (DLS) with a Nanotrac 150 particle size analyzer (Microtrac, Inc.,
453 Montgomeryville, PA) and geometric eight-root regression, with no residuals, was used to fit the
454 data. The nano-range option was selected and a scan time of 90 seconds was used.

455 Transverse relaxation times (T_2) of the VDIO-DOTA particles were measured at 60 MHz (1.4 T)
456 and 37 °C on a BrukerMinispec mq60. The relaxivity was given as the slope of the straight line
457 plotted as the function of $1/T_2$ vs iron concentration. DIO and VDIO-DOTA were diluted in pH 7.0
458 deionized water to give five aqueous solutions (300 μL each): 10.5, 5.25, 2.625, 1.313, and 0.656 mg
459 Fe/L, respectively. Iron concentrations in each dilution were determined using Atomic Absorption
460 Spectroscopy. T_2 values were measured using a Carr-Purcell-Meiboom-Gill (CPMG) sequence with
461 $\tau = 1$ ms, and 200 data points. Each solution was incubated at 37°C for 5 minutes before
462 measurement.

463 *5.3 Cytotoxicity*

464 Cytotoxicity of VDIO-DOTA was evaluated on HepG2 liver cells using C_{12} – Resazurin
465 viability assays. HepG2 liver cells were cultured and maintained in Minimum Essential Medium
466 containing 10% FBS, 200 U/mL penicillin, 200 μg/mL streptomycin, 1 mM sodium pyruvate, and 1
467 mM nonessential amino acids at 37°C in a humidified 5% CO_2 atmosphere. Cells were plated in
468 96-well dishes at a concentration of 1 x 10^4 cells per well and incubated overnight (5% CO_2, 37°C).
469 After overnight incubation, media was replaced with fresh media containing VDIO-DOTA
470 nanoparticles of varying concentration (0, 0.04, 0.2, 1, 4 and 10mM iron). Each concentration was
471 performed in triplicate for statistical relevance. Cells were also treated with DIO nanoparticles
472 under the same conditions as control. Cells were plated in three 96-well plates for measurements at
473 time points of 4h, 24h and 48h. At each time point, nanoparticle solutions were removed and cells
474 were washed with 1X PBS for three times. Then fresh media containing C_{12} – Resazurin (5μM) was
475 added to each well of cells. After 15min of incubation, fluorescence was measured using a Safire
476 monochromator microplate reader (Tecan Austria G.M.B.H., Austria) with excitation of 563nm and
477 emission of 587nm.

478 *5.4 Iron staining*

479 Slides from the inflamed carotid were stained to evaluated for iron within the plaques using
480 Prussian Blue Solution[32], a 1:1 mixture of 3% hydrochloride acid solution and 3% potassium
481 ferrocyanide solution, to detect ferric ion (Fe^{3+}) in the tissue. Any ferric ion present in the tissue
482 reacted with the ferrocyanide and results in the formation of the bright blue pigment, Prussian blue,
483 or ferric ferrocyanide. First, slides were deparaffinized by toluene and rehydrated through changes
484 of ethanol with decreasing concentrations (100%, 95% and 75%). After rinsing, slides were placed in
485 Prussian blue solution for 30 min followed by a rinsing step to remove excess staining. Then
486 Nuclear Fast Red Staining was used to counterstain other tissue (pink) for 10 min. After
487 dehydration with alcohol and clearing with toluene, tissue sections were placed under coverslips on
488 slides with mounting media.

489 *5.5 Immunohistochemistry (IHC)*

490 The tissue sections were stained for inflammatory marker VCAM-1. The deparaffinization and
491 dehydration process were the same as that of iron staining. Antigen retrieval was performed to
492 unmask binding sites of the primary antibodies. Heat Induced Epitope Retrieval (HIER) was

performed using a Decloaking Chamber. 500 ml of deionized water was added into the chamber. A plastic staining jar with tissue slides immersed in Antigen Retrieval Solution (Sigma 10X Tris-HCl buffer, pH10, product #T6455) was placed in the Decloaker chamber. The Decloaker was programed for 30 seconds at 125 °C followed by 10 seconds at 85 °C at 22.5 psi. After the heating process was done, the staining jar was removed from the Decloaker and cooled for 15 minutes followed by TBST rinse (Fisher 20X Tris buffered saline with Tween-20 used as 1X diluted solution). Then endogenous peroxidase block was performed by using 3% H_2O_2 in water to cancel the interference of peroxidase in the final step.[33] Protein block buffer (Dako Protein Block) was used to treat the tissue slides to mask the non-specific binding sites. Samples were labeled using an indirect method. Anti-VCAM-1 antibody (Rabbit monoclonal [EPR5047] to VCAM-1, Abcam Inc., MA) was used as primary antibody to detect the VCAM-1 expression. Ready-to-use polymers carrying horseradish peroxidase (Dako North America, Inc., Carpinteria, CA) were then used as the secondary antibody. In the final staining step, peroxidase on the polymers reacted with hydrogen peroxide to reduce the DAB (3,3'-Diaminobenzidine) substrate and generate a brown product in regions of VCAM-1 expression. Slides were examined under microscope.

5.6 Animal Studies

5.6.1 Animal model

All animal studies were performed under protocols approved by the Animal Care and Use Committee of the University of California, Davis and the California Institute of Technology. Female C57BL/6 ApoE-/- (10 weeks old, Jax West Laboratories, West Sacramento, CA) mice were used for the experiments as described in previous studies.[14] Eight days prior to imaging, the left carotid artery of each mouse was ligated. Eight days was chosen because prior studies showed that VCAM-1 expression peaks between 7 and 10 days post-ligation in ApoE-/- mice.[34] At this stage pronounced plaques have not yet formed, but inflammation is evident. To perform the ligation a medial incision was made between the mandible and clavicle, exposing the glands and vessels of the neck. The carotid artery was singled out from the surrounding tissue, while protecting and excluding the parallel-running vagus nerve. A 6/0 silk suture was threaded under the dorsal side of the carotid artery and was tied off to cause injury to the site. The procedure was concluded with five to six interrupted 4/0 Ethicon (Ethicon Inc) suture to re-approximate the skin of the original ventral incision. The mice were monitored twice a day for approximately four days to check for irritation and to administer analgesics when appropriate. Subsequent to ligation, mice were placed on a high fat diet for seven days. (TD 88137, Harlan Laboratories Inc, Madison, WI).

5.6.2 *In vivo* MRI-only studies

MRI experiments were performed to determine the optimal injection dosages for the NPs prior to radiolabeling. Prior to NP injection, a pre-scan was taken as baseline. Then VDIO at dosages of 6 mg Fe/kg body mass, 30 mg Fe/kg and 60 mg Fe/kg, were injected intravenously via the tail vein catheter (N = 4 per concentration). Images were acquired at 4 and 24 hours post-injection.

All images were acquired on a 7T (Bruker Biospec) small animal scanner using a home built quadrature RF volume coil (Cleveland, OH). For all time points, the animal was anesthetized with a 1.5% isoflurane: air mixture and kept at 35–37 °C with warm air flowing through the bore while the respiration was monitored (MP150, Biopac, Goleta, CA). After localizing the region of interest (ROI) around the neck using a RARE spin echo sequence (TR/TE = 4000/22 ms, matrix size = 128 × 128, FOV = 35.35 × 35.35 mm², slice thickness = 0.754 mm), the common carotid arteries were located with a time-of-flight angiography sequence with venous saturation (FL2D_ANGIO method, Paravision 4.0: TR/TE = 13.7/3.5 ms, matrix size = 150 × 100; zero-filled to 256 × 100, FOV = 30 × 20 mm², slice thickness = 0.754 mm). A T_{2*} weighted multiple-gradient echo sequence was then utilized to visualize the uptake of nanoparticles (TR/TE = 718/3, 7, 11, 15, 19, 23 ms, F.A. = 25°, matrix size = 175 × 100; zero-filled to 234 × 133, FOV = 35 × 20 mm², slice thickness = 0.754 mm) at the region of the common carotid arteries.

542   5.6.3 *In vivo* PET/MRI imaging

543   Studies were performed using an integrated small animal PET/MRI system, consisting of a
544 first-generation MR-compatible PET insert (constructed by Simon Cherry et. al at UC Davis) that is
545 fitted within a 7T small animal MRI scanner. [16, 17] This enabled simultaneous PET/MRI images to
546 be acquired.

547   Mice (N = 4) were surgically prepared as described above. Pre-scans were obtained with MRI
548 as baseline. Next, mice were injected intravenously via the tail vein with 30 mg Fe/kg
549 VDIO-^{64}Cu-DOTA (~700uCi per mouse, 92% radiation yield) followed by a 150 μL of saline flush.
550 The activity of the injected dose was confirmed by measuring the difference in radioactivity
551 contained in the syringe before and after injection on a dose calibrator. Imaging was subsequently
552 performed at 4 and 24 hours post-injection. MRI images were acquired identically to the MRI-only
553 studies. PET images were acquired with scan duration of 600 seconds at the 4 hour time point and
554 300 seconds at the 24 hour time point. Images were reconstructed and co-registered to the MRI
555 dataset as previously described.[17, 35]

556   To compare the focal NP uptake between time points, dosage and subjects, we calculated a
557 contrast ratio (CR) metric as previously described.[36] This normalizes particle uptake at the
558 ligation site between subjects and factors out the signal contribution due to blood borne particles by
559 comparison with the contralateral control.

560   Briefly, CR is defined as:

561
$$CR = \left| \frac{\left[\frac{[I_{ligated}] - [I_{background}]}{[I_{control}] - [I_{background}]} \right]_i}{\left[\frac{[I_{ligated}] - [I_{background}]}{[I_{control}] - [I_{background}]} \right]_{prescan}} \right|$$

562 Where $I_{ligated}$ is the mean intensity of the ROI drawn around the ligated carotid artery, $I_{control}$ is the
563 mean intensity of the ROI drawn around the contra-lateral carotid. $I_{background}$ is the mean intensity of
564 the ROI drawn in the spinal cord at the same image slice as the other ROIs and i is either 4 or 24
565 hours post-injection time points. ROIs were drawn manually at slice levels approximately located at
566 the common carotid arteries. These were matched between time points. Angiography images were
567 used to guide ROI delineation around the carotid arteries. Because previous reports noted that the
568 carotid vessels along with the wall are ~1 mm in diameter,[36] all arterial ROIs had diameters of 1.5
569 mm.

570   Representative region of interests used for CR calculation are indicated in Figure 3. Values
571 greater than 1 indicate localization at the ligation site. The T_{2^*} weighted image sets at TE = 11 ms
572 were used. All images were analyzed using ImageJ.

573   5.6.4 Visualization of image volumes

574   We developed a hardware accelerated volume rendering system with enhanced rendering
575 quality to provide better visualization of the PET and MRI signal at the site of the inflamed arteries.
576 To provide anatomical context, we superimpose a cross section of the data. Illustrative
577 rendering[37] is applied to this cross section for relative spatial position of the target vessel. The
578 vessel ROIs were manually segmented from the MRI images to identify the vessel walls. A
579 pre-integrated transfer function[38] was used to visualize the thin layer of vessel wall as a smooth
580 and continuous surface. To highlight the NP uptake on the surface of the arteries, we used a color
581 map to sort the surface MR signal ranging from red (low MR signal), through blue (medium) to
582 light pink (high MR).

583   *5.7 Histology*

584   After the *in vivo* animal study, organs known to be involved in disease or clearance, i.e. hearts,
585 carotid arteries, kidneys, spleens and livers, were collected and used for histology. The tissue was

fixed in 4% formaldehyde, and then dehydrated by passing tissue through increasing concentrations of ethanol (75%, 95% and 100%). Then the tissue was placed in warm paraffin wax, and the melted wax filled the spaces that used to contain water. After cooling, the tissue hardened into a paraffin block from which 5-micron tissue slices were sectioned and mounted on glass slides. The tissue sections were stained for iron and VCAM-1 as detailed in Supplemental Information.

Supplementary Materials: N/A

Author Contributions: AYL conceived and designed experiments; SD, TN, AH, TT, CT contributed to experiment design, performed experiments and contributed to data analysis; LZ prepared computer programs to render the imaging data; JP, IE performed and provided training for histology; REJ, KP contributed to experimental design and data analysis.

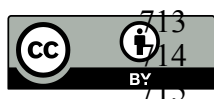**Conflicts of Interest:** The authors declare no conflict of interest.

References

1. Fuster V, Lois F, Franco M. Early identification of atherosclerotic disease by noninvasive imaging. Nature Reviews Cardiology. 2010;7(6):327-33.
2. Finn AV, Nakano M, Narula J, Kolodgie FD, Virmani R. Concept of vulnerable/unstable plaque. Arteriosclerosis, thrombosis, and vascular biology. 2010;30(7):1282-92.
3. Kolodgie FD, Burke AP, Skorija KS, Ladich E, Kutys R, Makuria AT, et al. Lipoprotein-associated phospholipase A2 protein expression in the natural progression of human coronary atherosclerosis. Arteriosclerosis, thrombosis, and vascular biology. 2006;26(11):2523-9.
4. Braganza D, Bennett M. New insights into atherosclerotic plaque rupture. Postgraduate medical journal. 2001;77(904):94-8.
5. DeMarco JK, Huston III J. Imaging of high-risk carotid artery plaques: current status and future directions. Neurosurgical focus. 2014;36(1):E1.
6. Cai J-M, Hatsukami TS, Ferguson MS, Small R, Polissar NL, Yuan C. Classification of human carotid atherosclerotic lesions with in vivo multicontrast magnetic resonance imaging. Circulation. 2002;106(11):1368-73.
7. Hyafil F, Schindler A, Sepp D, Obenhuber T, Bayer-Karpinska A, Boeckh-Behrens T, et al. High-risk plaque features can be detected in non-stenotic carotid plaques of patients with ischaemic stroke classified as cryptogenic using combined F-18-FDG PET/MR imaging. European Journal of Nuclear Medicine and Molecular Imaging. 2016 Feb;43(2):270-9.
8. Moon SH, Cho YS, Noh TS, Choi JY, Kim BT, Lee KH. Carotid FDG Uptake Improves Prediction of Future Cardiovascular Events in Asymptomatic Individuals. Jacc-Cardiovascular Imaging. 2015 Aug;8(8):949-56.
9. van der Valk FM, Verweij SL, Zwinderman KAH, Strang AC, Kaiser Y, Marquering HA, et al. Thresholds for Arterial Wall Inflammation Quantified by F-18-FDG PET Imaging. Jacc-Cardiovascular Imaging. 2016 Oct;9(10):1198-207.
10. Yarasheski KE, Laciny E, Overton ET, Reeds DN, Harrod M, Baldwin S, et al. (18)FDG PET-CT imaging detects arterial inflammation and early atherosclerosis in HIV-infected adults with cardiovascular disease risk factors. J Inflamm (Lond). 2012;9:26.
11. Huet P, Burg S, Le Guludec D, Hyafil F, Buvat I. Variability and Uncertainty of F-18-FDG PET Imaging Protocols for Assessing Inflammation in Atherosclerosis: Suggestions for Improvement. Journal of Nuclear Medicine. 2015 Apr;56(4):552-9.

635 12. van der Valk FM, Verweij SL, Zwinderman KA, Strang AC, Kaiser Y, Marquering HA, et al. Thresholds
636   for Arterial Wall Inflammation Quantified by 18F-FDG PET Imaging: Implications for Vascular
637   Interventional Studies. JACC Cardiovasc Imaging. 2016 Oct;9(10):1198-207.
638 13. Brammen L, Steiner S, Berent R, Sinzinger H. Molecular imaging of atherosclerotic lesions by positron
639   emission tomography - can it meet the expectations? Vasa-European Journal of Vascular Medicine.
640   2016;45(2):125-32.
641 14. Jarrett BR, Correa C, Ma KL, Louie AY. In vivo mapping of vascular inflammation using multimodal
642   imaging. PloS one. 2010;5(10):e13254.
643 15. Schindler TH. Cardiovascular PET/MR imaging: Quo Vadis? J Nucl Cardiol. 2016 Sep 22.
644 16. Catana C, Procissi D, Wu Y, Judenhofer MS, Qi J, Pichler BJ, et al. Simultaneous in vivo positron emission
645   tomography and magnetic resonance imaging. Proceedings of the National Academy of Sciences.
646   2008;105(10):3705-10.
647 17. Ng TS, Bading JR, Park R, Sohi H, Procissi D, Colcher D, et al. Quantitative, simultaneous PET/MRI for
648   intratumoral imaging with an MRI-compatible PET scanner. Journal of Nuclear Medicine.
649   2012;53(7):1102-9.
650 18. Nahrendorf M, Jaffer FA, Kelly KA, Sosnovik DE, Aikawa E, Libby P, et al. Noninvasive vascular cell
651   adhesion molecule-1 imaging identifies inflammatory activation of cells in atherosclerosis. Circulation.
652   2006;114(14):1504-11.
653 19. Broisat A, Toczek J, Dumas LS, Ahmadi M, Bacot S, Perret P, et al. Tc-99m-cAbVCAM1-5 Imaging Is a
654   Sensitive and Reproducible Tool for the Detection of Inflamed Atherosclerotic Lesions in Mice. Journal of
655   Nuclear Medicine. 2014 Oct;55(10):1678-84.
656 20. Dimastromatteo J, Broisat A, Perret P, Ahmadi M, Boturyn D, Dumy P, et al. In Vivo Molecular Imaging
657   of Atherosclerotic Lesions in ApoE(-/-) Mice Using VCAM-1-Specific, Tc-99m-Labeled Peptidic
658   Sequences. Journal of Nuclear Medicine. 2013 Aug;54(8):1442-9.
659 21. Wu J, Leong-Poi H, Bin J, Yang L, Liao Y, Liu Y, et al. Efficacy of Contrast-enhanced US and Magnetic
660   Microbubbles Targeted to Vascular Cell Adhesion Molecule–1 for Molecular Imaging of Atherosclerosis.
661   Radiology. 2011;260(2):463-71.
662 22. Ripa RS, Kj, #xe6, r A. Imaging Atherosclerosis with Hybrid Positron Emission Tomography/Magnetic
663   Resonance Imaging. BioMed Research International. 2015;2015:8.
664 23. O'Brien J, Wilson I, Orton T, Pognan F. Investigation of the Alamar Blue (resazurin) fluorescent dye for
665   the assessment of mammalian cell cytotoxicity. European Journal of Biochemistry. 2000;267(17):5421-6.
666 24. Petersen C, Peçanha PB, Venneri L, Pasanisi E, Pratali L, Picano E. The impact of carotid plaque presence
667   and morphology on mortality outcome in cardiological patients. Cardiovasc Ultrasound. 2006;4(16).
668 25. Wilson CM. Synthesis of Ultrasmall Superparamagnetic Iron Oxide Nanoparticles for fMRI.
669 26. Jarrett BR, Frendo M, Vogan J, Louie AY. Size-controlled synthesis of dextran sulfate coated iron oxide
670   nanoparticles for magnetic resonance imaging. Nanotechnology. 2007;18(3):035603.
671 27. Wunderbaldinger P, Josephson L, Bremer C, Moore A, Weissleder R. Detection of lymph node metastases
672   by contrast-enhanced MRI in an experimental model. Magnetic resonance in medicine. 2002;47(2):292-7.
673 28. Tu C, Ng TS, Jacobs RE, Louie AY. Multimodality PET/MRI agents targeted to activated macrophages.
674   JBIC Journal of Biological Inorganic Chemistry. 2014;19(2):247-58.
675 29. Josephson L, Kircher MF, Mahmood U, Tang Y, Weissleder R. Near-infrared fluorescent nanoparticles as
676   combined MR/optical imaging probes. Bioconjugate chemistry. 2002;13(3):554-60.
677 30. Gustafsson B, Youens S, Louie AY. Development of contrast agents targeted to macrophage scavenger
678   receptors for MRI of vascular inflammation. Bioconjugate chemistry. 2006;17(2):538-47.
679 31. Anderegg G, Arnaud-Neu F, Delgado R, Felcman J, Popov K. Critical evaluation of stability constants of
680   metal complexes of complexones for biomedical and environmental applications*(IUPAC Technical
681   Report). Pure and applied chemistry. 2005;77(8):1445-95.
682 32. Sheehan DC, Hrapchak BB. Theory and practice of histotechnology: Mosby St. Louis; 1980.
683 33. Streefkerk J. Inhibition of erythrocyte pseudoperoxidase activity by treatment with hydrogen peroxide
684   following methanol. Journal of Histochemistry & Cytochemistry. 1972;20(10):829-31.
685 34. Barringhaus KG, Phillips JW, Thatte JS, Sanders JM, Czarnik AC, Bennett DK, et al. α4β1 Integrin (VLA-4)
686   Blockade Attenuates both Early and Late Leukocyte Recruitment and Neointimal Growth following
687   Carotid Injury in Apolipoprotein E (–/–) Mice. Journal of vascular research. 2004;41(3):252-60.

688 35. Ng TS, Procissi D, Wu Y, Jacobs RE. A robust coregistration method for in vivo studies using a first
689   generation simultaneous PET/MR scanner. Medical physics. 2010;37(5):1995-2003.
690 36. Tu C, Ng TS, Sohi HK, Palko HA, House A, Jacobs RE, et al. Receptor-targeted iron oxide nanoparticles
691   for molecular MR imaging of inflamed atherosclerotic plaques. Biomaterials. 2011;32(29):7209-16.
692 37. Lum EB, Ma K-L, editors. Hardware-accelerated parallel non-photorealistic volume rendering.
693   Proceedings of the 2nd international symposium on Non-photorealistic animation and rendering; 2002:
694   ACM.
695 38. Lum EB, Wilson B, Ma K-L, editors. High-quality lighting and efficient pre-integration for volume
696   rendering. Proceedings of the Sixth Joint Eurographics-IEEE TCVG conference on Visualization; 2004:
697   Eurographics Association.
698 39. Bashir U, Mallia A, Stirling J, Joemon J, MacKewn J, Charles-Edwards G, et al. PET/MRI in Oncological
699   Imaging: State of the Art. Diagnostics. 2015;5(3):333-57.
700 40. Partovi S, Kohan A, Rubbert C, Vercher-Conejero JL, Gaeta C, Yuh R, et al. Clinical oncologic applications
701   of PET/MRI: a new horizon. Am J Nucl Med Mol Imaging. 2014;4(2):202-12.
702 41. Catalano OA, Rosen BR, Sahani DV, Hahn PF, Guimaraes AR, Vangel MG, et al. Clinical impact of
703   PET/MR imaging in patients with cancer undergoing same-day PET/CT: initial experience in 134
704   patients--a hypothesis-generating exploratory study. Radiology. 2013 Dec;269(3):857-69.
705 42. Nensa F, Schlosser T. Cardiovascular hybrid imaging using PET/MRI. Rofo. 2014 Dec;186(12):1094-101.
706 43. Li X, Heber D, Rausch I, Beitzke D, Mayerhoefer ME, Rasul S, et al. Quantitative assessment of
707   atherosclerotic plaques on 18F-FDG PET/MRI: comparison with a PET/CT hybrid system. Eur J Nucl Med
708   Mol Imaging. 2016;43:1503-12.
709 44. Masuda A, Yamaki T, Sakamoto N, Kunii H, Ito H, Nanbu T, et al. Vulnerable plaque on the common
710   iliac artery detected by F-18-FDG PET/MRI. European Journal of Nuclear Medicine and Molecular
711   Imaging. 2016 Apr;43(4):793-4.
712